Volume 10
Number 8
28 February 2022
Pages 1139–1320

Journal of Materials Chemistry B

Materials for biology and medicine

rsc.li/materials-b

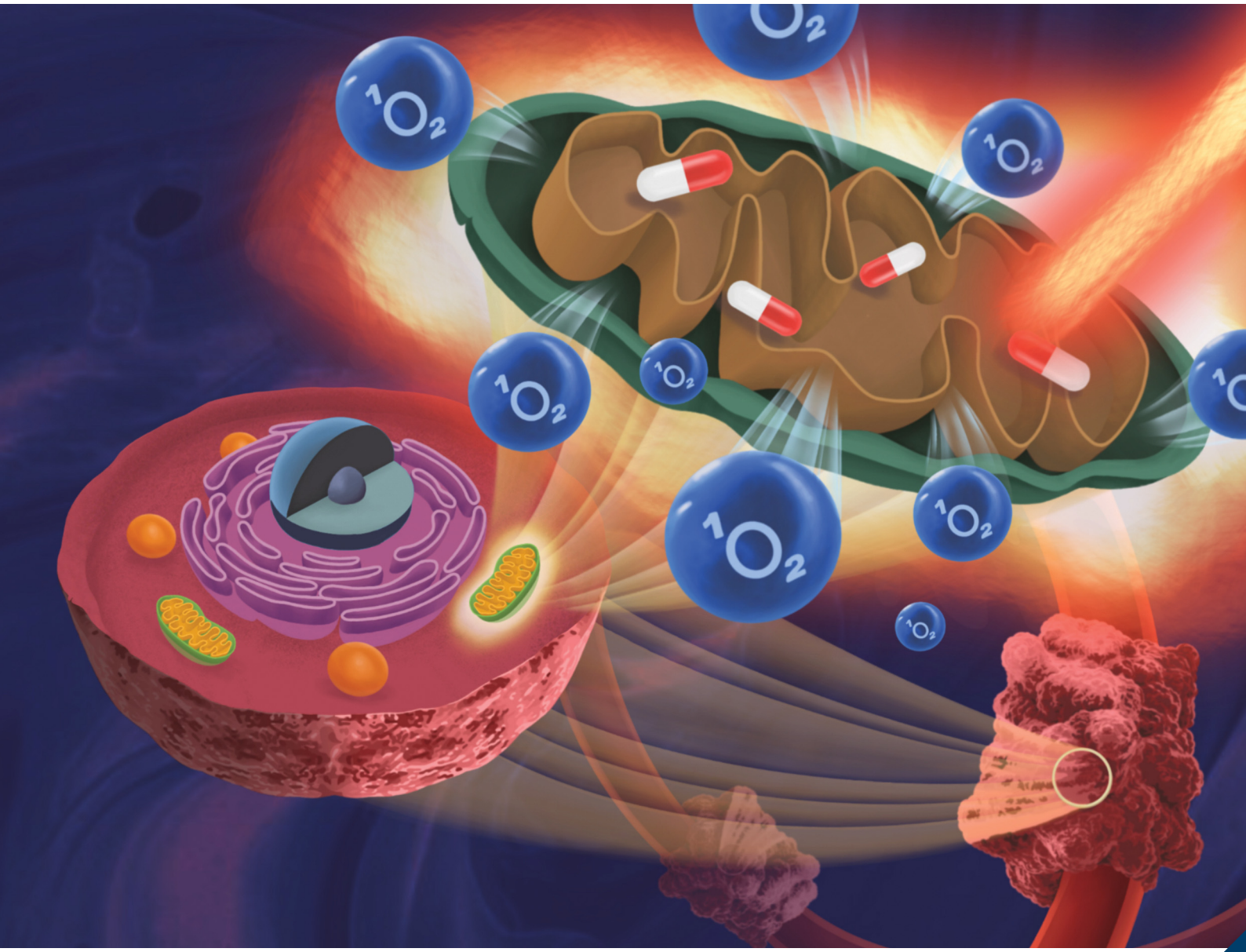

ISSN 2050-750X

ROYAL SOCIETY OF CHEMISTRY

PAPER

Joomin Lee, Ho-Joong Kim, Jaesung Yang *et al.*
Mitochondrion-targeting PEGylated BODIPY dyes for near-infrared cell imaging and photodynamic therapy

Indexed in Medline!

Journal of Materials Chemistry B

ROYAL SOCIETY OF CHEMISTRY

PAPER

View Article Online
View Journal | View Issue

Cite this: J. Mater. Chem. B, 2022, 10, 1196

Mitochondrion-targeting PEGylated BODIPY dyes for near-infrared cell imaging and photodynamic therapy†

Isabel Wen Badon, ‡[a] Chanwoo Kim, ‡[b] Jong Min Lim, ‡[c] Duy Khuong Mai,‡[ad] Temmy Pegarro Vales,[e] Dongho Kang,[b] Sung Cho,[d] Joomin Lee,*[f] Ho-Joong Kim*[a] and Jaesung Yang *[b]

Received 1st November 2021,
Accepted 17th January 2022

DOI: 10.1039/d1tb02393d

rsc.li/materials-b

A series of 4,4-difluoro-4-bora-3*a*,4*a*-diaza-*s*-indacene-based photosensitizers (AmB*X*I, X = H, M, Br) featuring a cationic mitochondrion-targeting group and near-infrared (NIR) absorption was synthesized. After extending the photosensitizers' π conjugation *via* Knoevenagel reaction, both the absorbance and emission maxima of AmB*X*I shifted to the phototherapeutic wavelength range (650–900 nm). Theoretical computations indicate that the introduction of bromine atoms promotes spin–orbit coupling, so that for each additional bromine atom in AmB*X*I an increase in singlet oxygen quantum yield would be expected (0.3%, 2.2%, and 4.1%, for AmBHI, AmBMI, and AmBBrI, respectively). Moreover, AmB*X*I photosensitizers exhibited low cytotoxicity in the dark and high phototoxicity, with the half maximal inhibitory concentrations of AmBBrI found to be 46.93 nM and 22.84 nM, while those of AmBMI were 129.7 nM and 58.34 nM in HeLa and MCF-7 cancer cells, respectively. Notably, introduction of a single bromine atom was enough to produce a cytotoxic effect. Furthermore, the presence of a quaternary ammonium group in AmB*X*I enabled the dyes to localize and stain the negatively charged mitochondria. The results presented herein indicate the straightforward and facile synthesis of NIR-light triggered mitochondrion-targeting photosensitizers.

Introduction

Photodynamic therapy (PDT) is a photochemistry-based health treatment that is minimally invasive, causes low toxicity in healthy tissues, and does not produce drug resistance, even after repeated implementations.[1,2] PDT has been proven effective against malignant and benign tumors, whether implemented as the primary treatment or in combination with other therapies.[3–5] In PDT, cytotoxic singlet oxygen ($^1O_2$) is generated as a result of the interaction of the three key components of the therapeutic approach: a photosensitizer (PS), light, and molecular oxygen ($^3O_2$). Initially, PSs are introduced in the target tissue; the said tissue is then subjected to light irradiation, triggering the excitation of the PS from the singlet ground state (S_0) to the singlet excited state (S_n). S_n can then relax back to the ground state or undergo intersystem crossing (ISC) to the triplet excited state (T_1), which can either activate the photochemical processes leading to the production and release of reactive free radicals or transfer its energy to ground-state $^3O_2$ species to produce $^1O_2$.[6] The $^1O_2$ thus generated can cause cancer cell death either by directly attacking these cells or by causing tumor vascular occlusions.[7] However, the $^1O_2$ quantum yield (ϕ_Δ) largely depends on the efficiency of the $S_1 \rightarrow T_1$ electronic transition, which is a spin-forbidden process. Attaching heavy atoms like iodine, bromine, or transition metals to the PS molecule promotes spin–orbit coupling (SOC) and increases the likelihood of the $S_1 \rightarrow T_1$ ISC. However, transition metals like iridium or ruthenium are expensive, and the ϕ_Δ value achieved using them is no higher than that obtained using halogens.[8] Moreover, the low tissue penetration depth achieved by visible light presents another practical limitation to the use of PDT in biological applications. In fact, tissue penetration is maximal for light characterized by wavelengths in the near-infrared (NIR) spectrum.[9] In this regard, PSs that

[a] Department of Chemistry, Chosun University, Gwangju 61452, Korea. E-mail: hjkim@chosun.ac.kr
[b] Department of Chemistry, Yonsei University, Wonju, Gangwon 26493, Korea. E-mail: jaesung.yang@yonsei.ac.kr
[c] Center for Molecular Spectroscopy and Dynamics, Institute for Basic Science (IBS), Seoul 02841, Korea
[d] Department of Chemistry, Chonnam National University, 99 Daehak-ro, Yuseong-gu, Gwangju 61186, Korea
[e] Department of Natural Sciences, Caraga State University, Butuan City 8600, Philippines
[f] Department of Food and Nutrition, Chosun University, Gwangju 61452, Korea

† Electronic supplementary information (ESI) available. See DOI: 10.1039/d1tb02393d

‡ These authors contributed equally to this work.

can be activated by electromagnetic waves falling within the "phototherapeutic window (650–900 nm)" are preferable.

Touted as "porphyrin's little sister," derivatives of 4,4-difluoro-4-bora-3*a*,4*a*-diaza-*s*-indacene (BODIPY) boast excellent photophysical properties, such as sharp absorption bands, high thermal and photochemical stability, and high fluorescence quantum yields, which make them ideal platforms for optical imaging and lasing, as well as for the manufacture of light-emitting diodes and dye-sensitized solar cells.[10–14] Their structures can also be tuned to accommodate synthetic demands. Needless to say, numerous BODIPY-based PSs have been developed.[15–22] Specifically, NIR-absorbing BODIPY derivatives are readily accessible *via* extension of the π-conjugation of the BODIPY core structure.[23] However, as a result of this strategy, the hydrophobicity of the overall structure is inadvertently increased, which is an undesirable outcome from the standpoint of biological applications, as rigid and lipophilic BODIPY-based compounds tend to localize in the intracellular membrane.[24,25] This problem can be overcome by introducing hydrophilic groups in the structure of the PS, such as polyethylene glycol, phosphonates, and sulfonates, whose presence offsets the increase in hydrophobicity associated with π-conjugation extension and prevents dye molecule aggregation within the cell.[26,27]

Nonspecific binding and off-target toxicity of compounds are serious bottlenecks in the development and approval of novel cancer drugs. The risk of causing deleterious effects on healthy tissues highlights the importance of identifying biomarkers or developing targeting strategies.[28–30] However, the variability in the degree of expression of genes and the presence of mutations even within the same tumor renders the targeting of a single gene or a single pathway a complex task to realize.[31,32] Notably, mitochondria are membrane-bound organelles that in healthy cells are mainly in charge of energy production, reactive oxygen species (ROS) production, macromolecular synthesis, and cell signaling activation.[33,34] In cancer cells, mitochondrial dysfunction is common, and it is associated with compromised oxidative phosphorylation, excess ROS production, calcium accumulation and inflammation. Mitochondrial dysfunction also promotes tumorigenesis and cancer cell progression and recurrence. Cancer cells are also characterized by a higher mitochondrial membrane potential than normal cells.[35] These distinctive features of dysfunctional mitochondria render them potential targeting sites for cancer treatment. In fact, several mitochondrion-targeting PSs feature cations in their structure, such as triphenylphosphonium and quaternary ammonium groups, which can exploit the mentioned difference in mitochondrial membrane potential to drive the preferential accumulation of the PSs in the mitochondria of cancer cells.[36,37] For example, molybdenum-based complexes functionalized with either TPP or methylpyridinium ligands have been shown to accumulate in HeLa cell mitochondria and exhibit phototoxicity toward the cells. However, these PSs have limitations, such as insufficient water solubility and poor cellular uptake.[36–44]

In view of the described concepts, we herein report the synthesis of NIR-absorbing BODIPY-based dyes featuring good water solubility and mitochondrion selectivity. The spectroscopic properties and $^1O_2$ generation efficiency of the mentioned fluorophores were also investigated. Computational studies were also conducted to understand the effects of the structural modifications of the dyes. The synthesized compounds were tested *in vitro* to investigate the practicality of using the dyes in living systems. Evidence suggested that they may enable users to achieve light-controlled cell death and a clear visualization of mitochondria within cells.

Results and discussion

In Scheme 1 is outlined the synthetic approach adopted to obtain BODIPY-based, NIR-absorbing dyes endowed with mitochondrion-targeting ability to be used in PDT. The applied design strategy was intended to circumvent the general

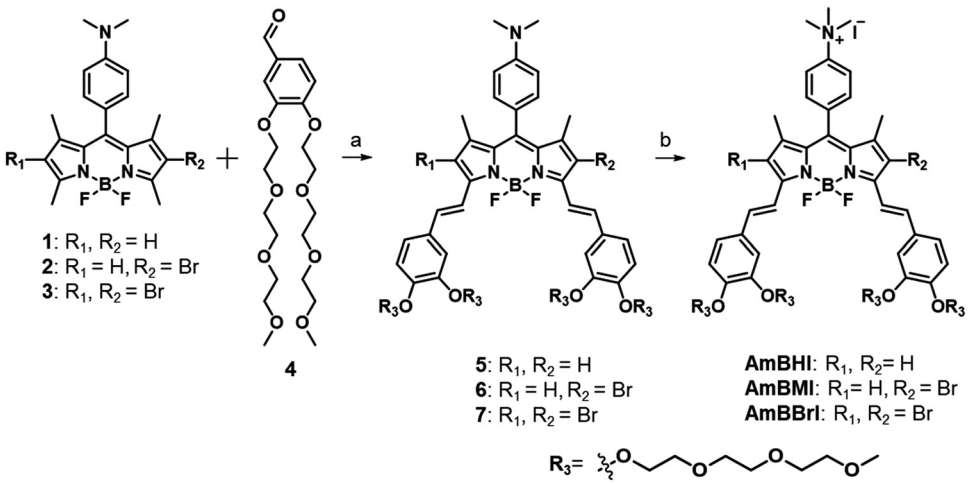

Scheme 1 Synthesis of mitochondrion-targeting 4,4-difluoro-4-bora-3*a*,4*a*-diaza-*s*-indacene-based photosensitizers AmBXI (X = H, M, Br). (a) Piperidine, acetic acid, dimethylformamide, reflux. (b) Iodomethane, acetonitrile, room temperature.

limitations associated with the use of BODIPY-based PSs by making full use of the sites available for modification. Initially, 2,4-dimethylpyrrole and (4-dimethyl)benzaldehyde were made to react at room temperature in the presence of trifluoroacetic acid acting as a catalyst. The reaction reached completion following the addition of 1,3-dichloro-5,6-dicyanobenzoquinone (DDQ), TEA, and $BF_3{\cdot}OEt_2$ under controlled conditions. The lateral 2,6 positions of the BODIPY core were then subjected to monobromination or dibromination. Benzaldehydes conjugated with two triethylene glycol (TEG) chains were made to react with the two acidic bottom methyl groups of the BODIPY core *via* a Knoevenagel condensation. Finally, a quantitative methylation of the dimethylanilino moiety produced an ammonium cation, which enhances the hydrophilicity of the dye and acts as mitochondrion-targeting active group. The three compounds thus obtained, listed in order of increasing number of conjugated bromine atoms, are referred to as AmBHI (0 bromine atoms), AmBMI (1) and AmBBrI (2).

Because of the presence of multiple TEG chains and ammonium cation, AmB*X*I dyes were easily soluble in water such that sample solutions with concentration as high as sub-millimolar could be prepared with little precipitation as assessed by eyes. Furthermore, dynamic light scattering measurements of AmB*X*I dyes in phosphate-buffered saline at concentration of 250 μM revealed no appreciable signal, indicating the absence of nanometer-sized particles resulting from dye aggregation and assuring the high solubility of the dyes in aqueous media. While discernible aggregates are not formed, π–π interactions between numbers of AmB*X*I dye molecules exist, particularly, at high concentrations, as reflected by concentration-dependent

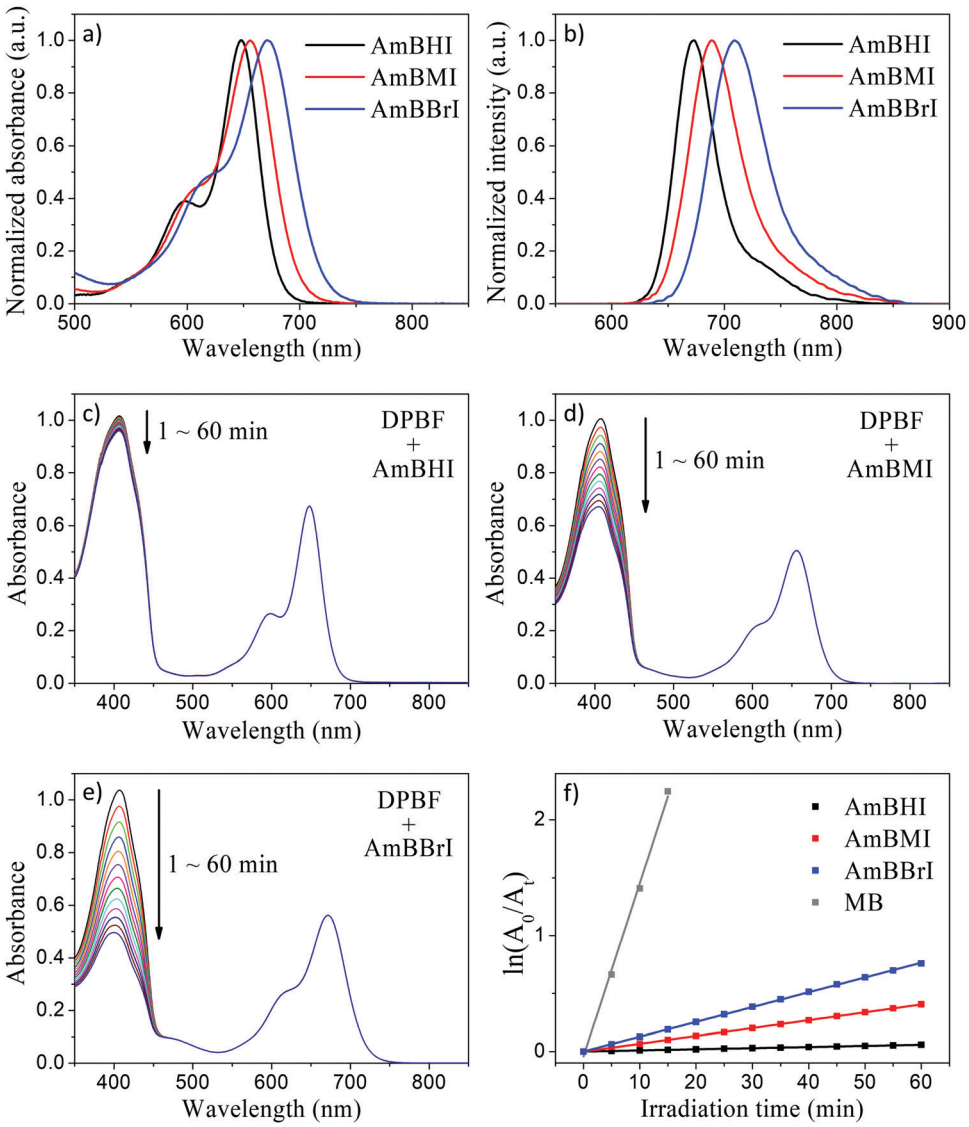

Fig. 1 Steady-state absorption (a) and emission (b) spectra of AmB*X*I dyes in methanol. Time-dependent absorption spectra of air-saturated DPBF methanol solutions containing AmBHI (c), AmBMI (d), and AmBBrI (e) obtained under the irradiation of 660 nm-LED light. (f) Temporal decrease in the absorbance of DPBF at 410 nm drawn according to the first-order kinetics (square dots) with linear fits (solid line) in semilogarithmic scale. MB: methylene blue.

spectral broadening and saturation in intensity of fluorescence spectra (see Fig. S1, ESI†).

The steady-state absorption and emission spectra of the synthesized BODIPY-based dyes are reported in Fig. 1a and b. Compared with compounds **1–3** (see Scheme 1), AmBHI, AmBMI, and AmBBrI exhibited a very dramatic redshift in absorption, so that the maximum absorbance was observed within the phototherapeutic window (650–850 nm). The observed λ_{max} value is in agreement with that previously reported for distyryl-BODIPY derivatives modified in the same fashion.[45] Notably, this success in the preparation of NIR-activatable PSs displaying excellent water solubility was achieved at the expense of the intensity of fluorescence emission. The attachment of two styryl units to the BODIPY core plays an essential role in the extension of π-conjugation, which led to the observed spectral redshift. However, free rotation is possible around the resultant vinyl bonds, which provides undesirable nonradiative decay pathways and induces fluorescence quenching. This rotation is likely to be boosted by a bundle of long, flexible TEG chains dangling from the styryl moieties. Hence, the fluorescence quantum yield (ϕ_F) of AmBHI was determined to be 0.18 (Table 1), which is half the typical value observed for unsubstituted BODIPY derivatives.[46,47] The further gradual decrease in ϕ_F value in going from AmBHI to AmBMI (0.11), and AmBBrI (0.06) is attributable to ISC, which becomes more efficient as the number of bromine atoms increases. We stress that despite the low value for ϕ_F, the halogenated BODIPY derivatives can still be used for cell imaging, as the evidence discussed below will indicate.

In order to evaluate the $^1O_2$-generation efficiency of AmB*X*I,1,3-diphenylisobenzofuran (DPBF) bleaching experiments were performed. Indeed, DPBF reacts with $^1O_2$ to yield 1,2-dibenzoylbenzene *via* a cycloaddition reaction. In turn, the oxidation of DPBF is made evident by a decrease in DPBF absorbance, which can be recorded as a simple strategy for quantifying the amount of $^1O_2$ species generated by PSs. In the relevant experiments, air-saturated methanol solutions of DPBF containing AmB*X*I were prepared, whereby the concentrations of both compounds were carefully controlled. The solutions were then irradiated with an LED light, while the absorption spectrum of DPBF was measured periodically. As can be evinced from Fig. 1c–e, a dramatic temporal decrease in the absorbance of DPBF was observed in the presence of AmBMI and AmBBrI. By contrast, only a trivial decrease was observed in the presence of AmBHI. The $^1O_2$ ϕ_Δ value was calculated assuming first-order kinetics using methylene blue (ϕ_Δ = 0.50 in methanol) as standard (Fig. 1f and Table 1). Compared to AmBHI, for which ϕ_Δ was as low as 0.4%, AmBMI and AmBBrI exhibited an order of magnitude enhancement in ϕ_Δ, with AmBBrI displaying the greatest efficiency (~4.5%). Consistent trend was observed for $^1O_2$ generation efficiency in water (Fig. S2, ESI†). Notably, the efficiency was observed to be directly proportional to the degree of bromination. The observed increase in ϕ_Δ of the halogenated BODIPY derivatives can be attributed to the heavy-atom effect.[48] Heavy atoms, like bromine employed here, boost the ISC process to bring more electrons into the triplet excited states through vibronic SOC.[45] The excited electrons, if necessary, relax to the lowest-energy triplet state and then collide with $^3O_2$ molecules to generate the highly reactive $^1O_2$ species, which ultimately destroy tumor cells. Essentially, the generation of $^1O_2$ depends on the efficiency of the ISC process.

In order to correlate the spectral properties of AmB*X*I dyes with their electronic structures, time-dependent density functional theory (TD-DFT) calculations were carried out at the B3LYP/6-31G(d) level of theory (see the Methods for computational details). As can be evinced from Fig. 2, the optimized geometries of the three dyes reveal that the BODIPY core and the two styryl moieties are almost coplanar in all compounds, resulting in HOMOs and LUMOs that are completely delocalized across both styryl moieties. The said coplanarity is barely

Table 1 Spectroscopic, photophysical, and photosensitizing properties of the herein synthesized 4,4-difluoro-4-bora-3*a*,4*a*-diaza-*s*-indacene-based dyes

	Experimental data				Calculated data		
	λ_{abs}[a] (nm)	λ_{em}[b] (nm)	ϕ_F[c]	ϕ_Δ[d]	S_1[e] (eV)	f[f]	Major contribution to the transition
AmBHI	648	673	0.18	0.004	2.09	1.0576	HOMO → LUMO (100%)
AmBMI	659	689	0.11	0.025	2.06	0.9907	HOMO → LUMO (100%)
AmBBrI	671	709	0.06	0.045	2.03	0.9410	HOMO → LUMO (100%)

[a] Wavelength of the maximum absorption. [b] Wavelength of the maximum fluorescence emission. [c] Fluorescence quantum yield determined with respect to rhodamine 6G in ethanol (ϕ_F = 0.95). [d] Singlet oxygen quantum yield determined using the DPBF bleaching method with methylene blue in methanol as standard (ϕ_Δ = 0.50). [e] Vertical excitation energy computed in water using B3LYP/6-31g(d). [f] Oscillator strength.

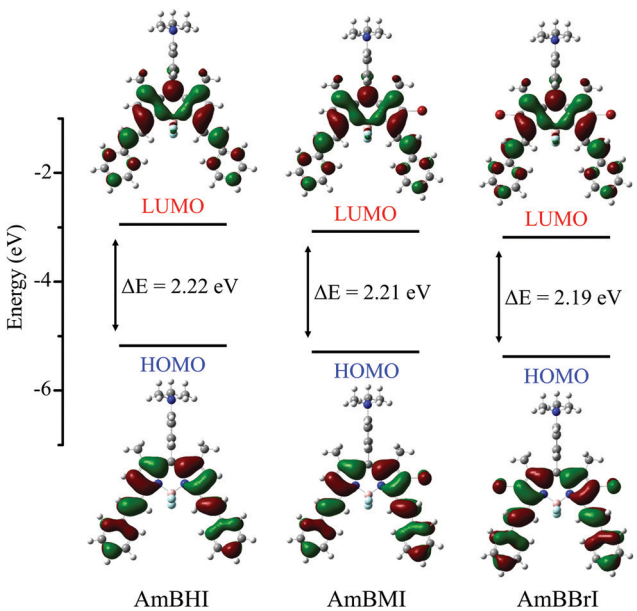

Fig. 2 Energy level diagrams and frontier molecular orbitals for the lowest-energy transitions of AmB*X*I dyes computed in water solvent using the B3LYP/6-31G(d) level of theory.

affected by the bulky peripheral chains, as indicated by the results of the geometry optimization of the complete structures of the AmB*X*I dyes (Fig. S3, ESI†). These data confirm the effective π-conjugation over the whole BODIPY backbone, which is the essential factor that shifts the spectral window of AmB*X*I dyes toward the NIR region. By taking a closer look at the HOMO of the halogenated BODIPY derivatives, one is able to confirm that the electron density spreads over the bromine atoms (Fig. 2), explaining the gradual bathochromic spectral shift observed upon going from AmBHI to AmBMI and AmBBrI (see Fig. 1a and b). Notably, with its orthogonal geometry, the trimethylanilino group in the meso position thwarts orbital overlap and π–π intramolecular interactions.[49,50]

In triplet PSs, $^1O_2$ generation must be preceded by the generation of triplet states, by which ϕ_Δ is directly related to the rate of ISC (k_{ISC}). A simplified description of k_{ISC} can be given as:[51]

$$k_{ISC} \propto \frac{\langle T_m|H_{SO}|S_n^2\rangle}{(\Delta E_{S_n-T_m})^2}$$

where H_{SO} is the Hamiltonian for the SOC and ΔE_{Sn-Tm} is the energy gap between singlet (S_n) and triplet (T_m) states. According to this equation, k_{ISC} is proportional to the square of the SOC matrix element and inversely proportional to the square of the energy gap between the states involved in the ISC. In this context, in order to estimate the value of k_{ISC} and identify the eventual presence of effective ISC channels for the AmB*X*I dyes, we calculated the SOC matrix elements for a manifold of S_n–T_m states and energies of excited states for the optimized geometries (see the Methods for computational details). As to the singlet states, only the S_1 state was considered in the calculations, since the ISC between S_n ($n > 1$) and triplet states is unlikely to occur, due to the fast internal conversion taking place, as indicated by Kasha's rule.[52] Moreover, the wavelength of the 660 nm-LED light used to conduct the singlet oxygen quantum yield measurements corresponds to the S_0–S_1 transition of AmB*X*I dyes.

In Fig. 3 are reported the SOC data and energy level diagrams with plausible photophysical decay pathways. For all compounds, the SOC values of the S_1–T_1 and S_1–T_3 manifolds are greater than that of the S_1–T_2 manifold. However, the values of ΔE_{S1-T1} and ΔE_{S1-T3} are too large (>0.65 eV) for the ISC process to occur, suggesting that the ISC between S_1 and T_m (m = 1, 3) states is improbable.[53] Among the triplet states, the T_2 state is closest in energy to the S_1 state; therefore, the S_1–T_2 manifold is the most likely candidate for the ISC channel of AmB*X*I dyes. The magnitudes of ΔE_{S1-T2} are similar across all AmB*X*I dyes, and they all fall in the 0.22–0.24 eV range, indicating a negligible influence of the energy difference on the kinetics of ISC. Unlike ΔE_{S1-T1}, the SOC values for the S_1–T_2 manifold are markedly different from each other. Although the SOC value of AmBHI is marginal (0.06 cm^{-1}), those of AmBMI and AmBBrI are larger (0.17 cm^{-1} and 0.28 cm^{-1}, respectively), confirming the heavy-atom effect associated with the introduction of bromine atoms in the BODIPY derivatives. These results indicate that in AmBMI and AmBBrI an ISC occurs efficiently between the S_1 and T_2 states; results also agree with the experimentally determined ϕ_Δ values for the AmB*X*I dyes. Overall, the steady-state spectroscopic and theoretical data indicate that the introduction of bromine atoms in the BODIPY core dramatically increases $^1O_2$ generation efficiency and demonstrate the high potential of the halogenated AmB*X*I dyes for application as PDT agents.

A confocal laser scanning microscopy experiment was carried out to determine the localization of AmB*X*I dyes inside the cell. Human cervical cancer (HeLa) cells were treated with AmB*X*I 1.0 μM for 24 h. As can be evinced from the images reported in Fig. 4a, the dyes accumulated in the cytoplasm of the HeLa cells (red areas) and were excluded from their nuclei (dark areas). TEG has been shown to significantly improve cellular retention.[54] Notably, AmBMI and AmBBrI, which exhibited reduced values for ϕ_F in aqueous solution relative to

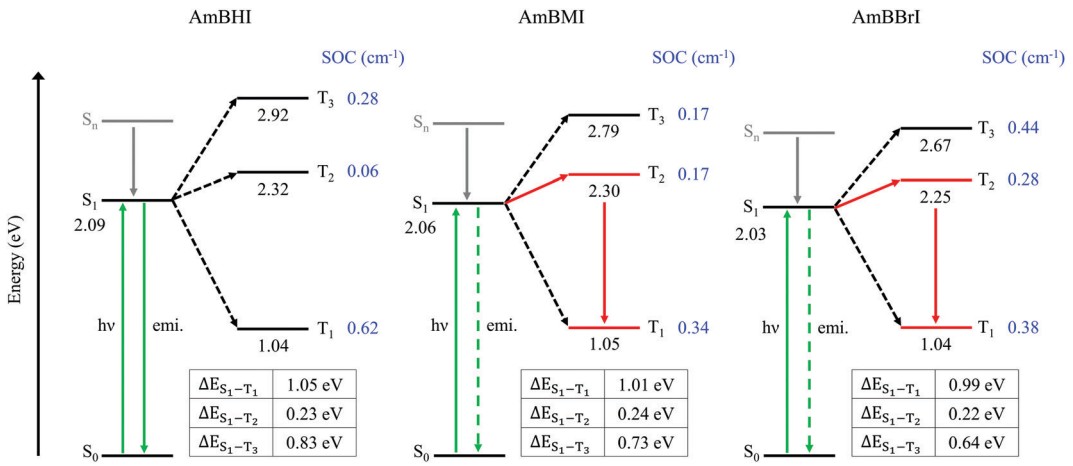

Fig. 3 Plausible photophysical decay pathways available for the photoexcited AmB*X*I dyes assessed on the basis of excited-state energies and spin–orbit coupling (SOC) values. The SOC values between the singlet S_1 and the triplet T_m (m = 1–3) states are presented in blue. In the tables are listed the values of the energy gaps between the S_1 and T_m (m = 1–3) states for each dye.

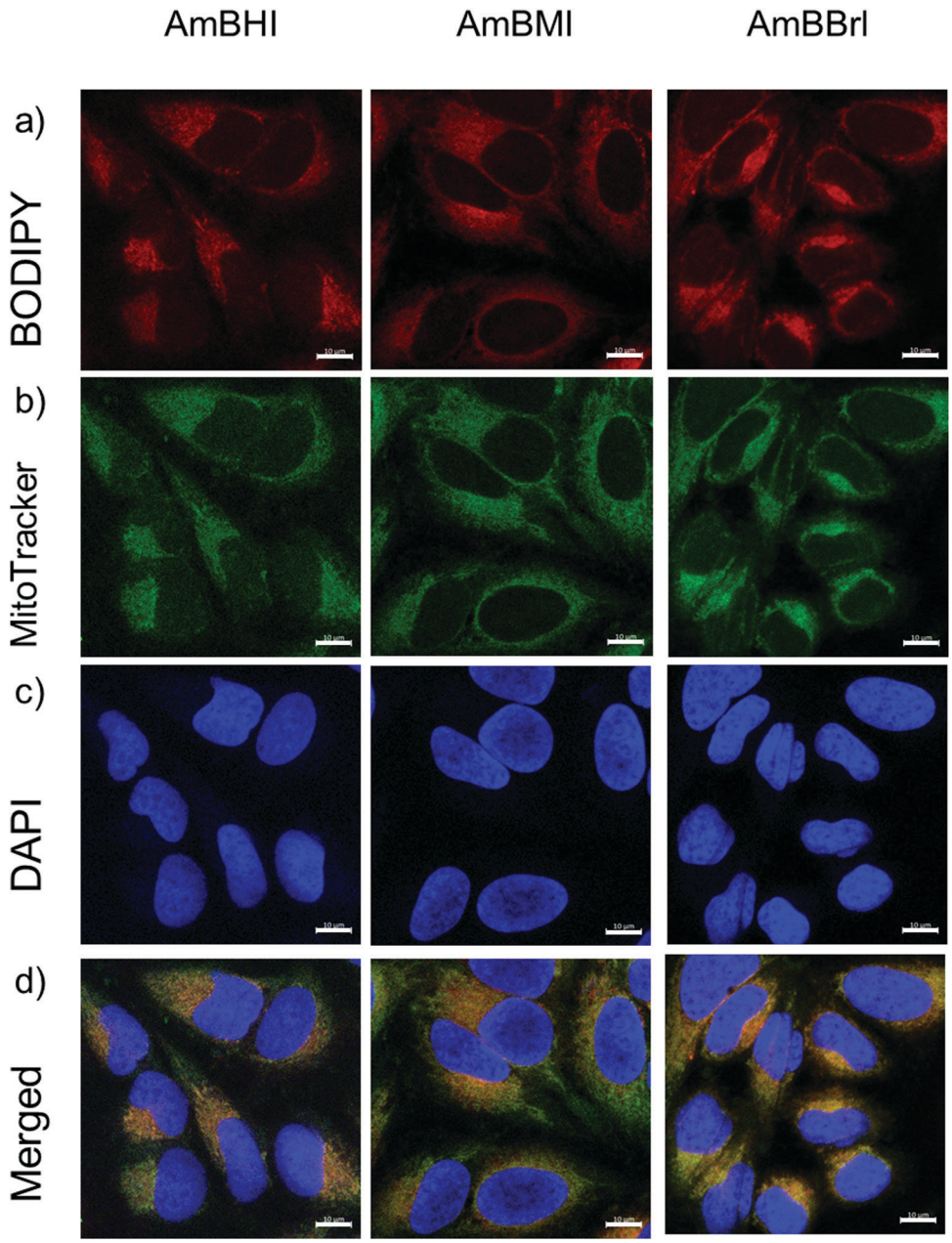

Fig. 4 Confocal laser scanning microscopy images of HeLa cells colabeled with AmBHI, AmBMI, and AmBBrI (a), MitoTracker Green (b), 4′,6-diamidino-2-phenylindole (DAPI) (c), and merged images (d). In all cases, the dye concentration was 1 μM. For cellular experiments, unless otherwise noted, the inactivated FBS and antibiotics were included when incubating cells with AmB*X*I dyes (see the Experimental section for more details). Scale: 10 μm.

AmBHI, exhibited fluorescence inside HeLa cells. Indeed, interactions between the AmB*X*I dyes and subcellular biomolecules may have hampered free rotation of the TEG chains and increased the molecular rigidity of the dyes, resulting in an enhanced fluorescence.[55] In order to verify the mitochondrion selectivity of AmB*X*I dyes, a multiple staining experiment was conducted utilizing the mitochondrial dye MitoTracker Green (Fig. 4b) and the nuclear dye 4′,6-diamidino-2-phenylindole (DAPI) (Fig. 4c). Merged images of the HeLa cells (Fig. 4d) indicated that the AmB*X*I colocalized with MitoTracker Green in the same region outside the DAPI-stained nuclei. A closer look at the superimposed fluorescence intensity profiles of AmB*X*I and MitoTracker Green dyes confirmed the congruence in the region of interest (Fig. 5). This evidence confirms the mitochondrion-specificity of AmB*X*I dyes. Gunbas *et al.* synthesized BODIPY-based PSs with cationic methyl pyridinium moieties, which displayed higher affinity for the mitochondria of HeLa cells than those of noncancerous NIH/3T3 cells.[44] The fact that the mitochondrial membrane of cancer cells is characterized by a higher potential than that of normal cells accounts for the preferential accumulation of cations in cancer cells.[56–58] Fluorescence activated cell sorting (FACS) analysis

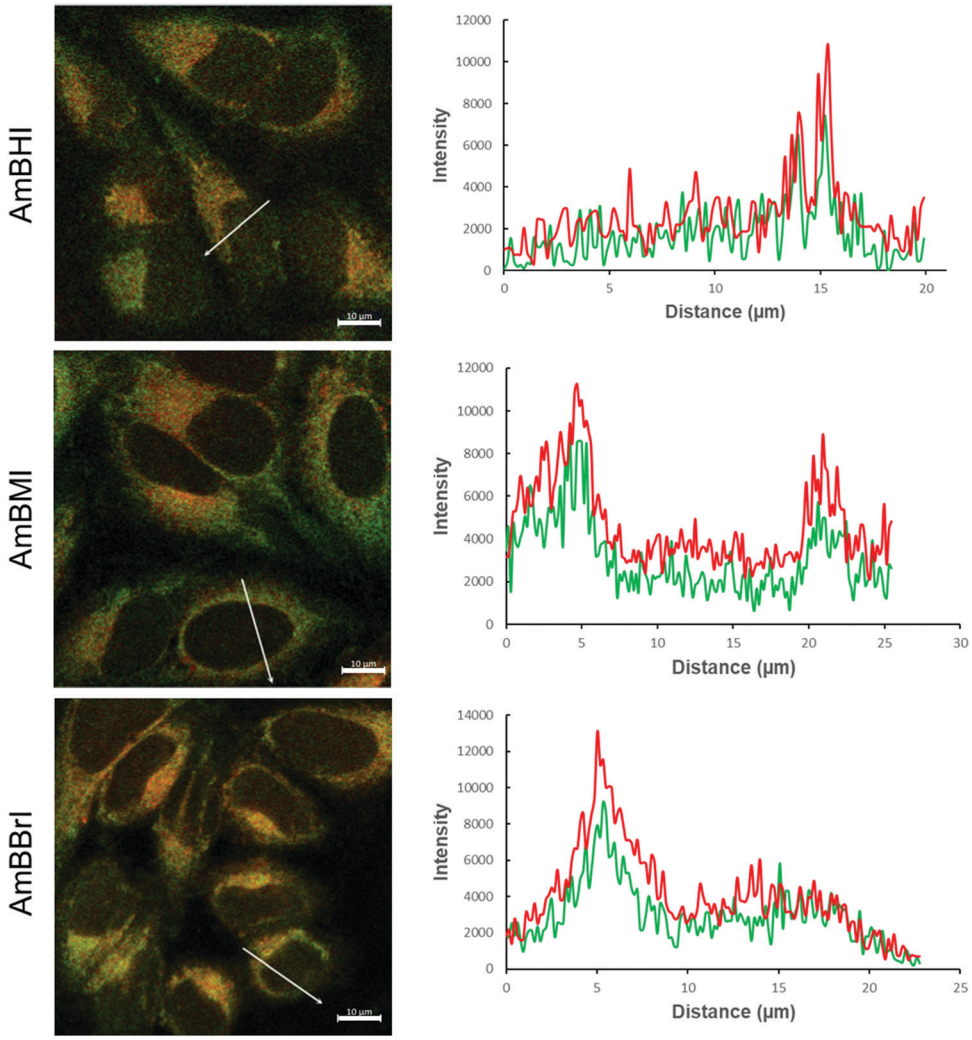

Fig. 5 Fluorescence intensity profile of AmBHI (top), AmBMI (middle), and AmBBrI (bottom), red profile, alongside that of MitoTracker Green (green profile) of the region of interest across the cell. Scale: 10 μm.

further evinced the entry of AmB*X*I dyes the cells (Fig. 6a and b). The corrected median intensity profiles against HeLa and MCF-7 cells shown in Table 2 indicate that the cells treated with AmB*X*I dyes exhibit more than 200-fold higher fluorescence emission than the untreated cells, with AmBHI producing the highest signal. These data show that the cationic dyes are well taken up by the mitochondria of the cancer cells. Similarly, AmBHI, AmBMI, and AmBBrI are expected to localize preferentially in cancer cells and direct their cytotoxic action against the mitochondria. Having established the cell permeability and biocompatibility of AmB*X*I dyes, these compounds were subjected to dose-dependent *in vitro* photosensitizing experiments using HeLa and human breast cancer (MCF-7) cells. The experiments were conducted in triplicate, and the relevant obtained results are summarized in Fig. 7. In the dark, both cell lines incubated with AmB*X*I dyes consistently exhibited high cell viability, up to a dye concentration of 640 nM; accordingly, AmB*X*I dyes were concluded to be characterized by low cytotoxicity in the absence of natural light. Note that when the dye concentration was further increased up to 1280 nM, the cell lines incubated with AmBHI exhibited a moderate reduction in cell viability down to 84.6% while incubation with halogenated dyes had little effect. After irradiation at 690 nm for 30 min, the cell viability of HeLa and MCF-7 cells treated with AmBHI remained $>80\%$. By contrast, cells treated with AmBBrI exhibited substantial reductions in viability, with a calculated IC_{50} values of 46.93 nM and 22.84 nM for HeLa and MCF-7 cells, respectively. In the case of AmBMI-treated cells, the phototoxic effect was moderate in comparison with AmBBrI, with calculated IC_{50} values of 129.7 nM and 58.34 nM for HeLa and MCF-7 cells, respectively.

To look deeper into the kinetics of cell death induced by AmB*X*I dyes, Annexin V/PI staining assay was conducted. This staining protocol is a sensitive method to quantify and differentiate between necrotic (unregulated) and apoptotic (programmed) cells. HeLa and MCF-7 cancer cells were treated with DMSO as control and AmB*X*I, respectively. The (early + late) apoptotic population was measured before and after LED

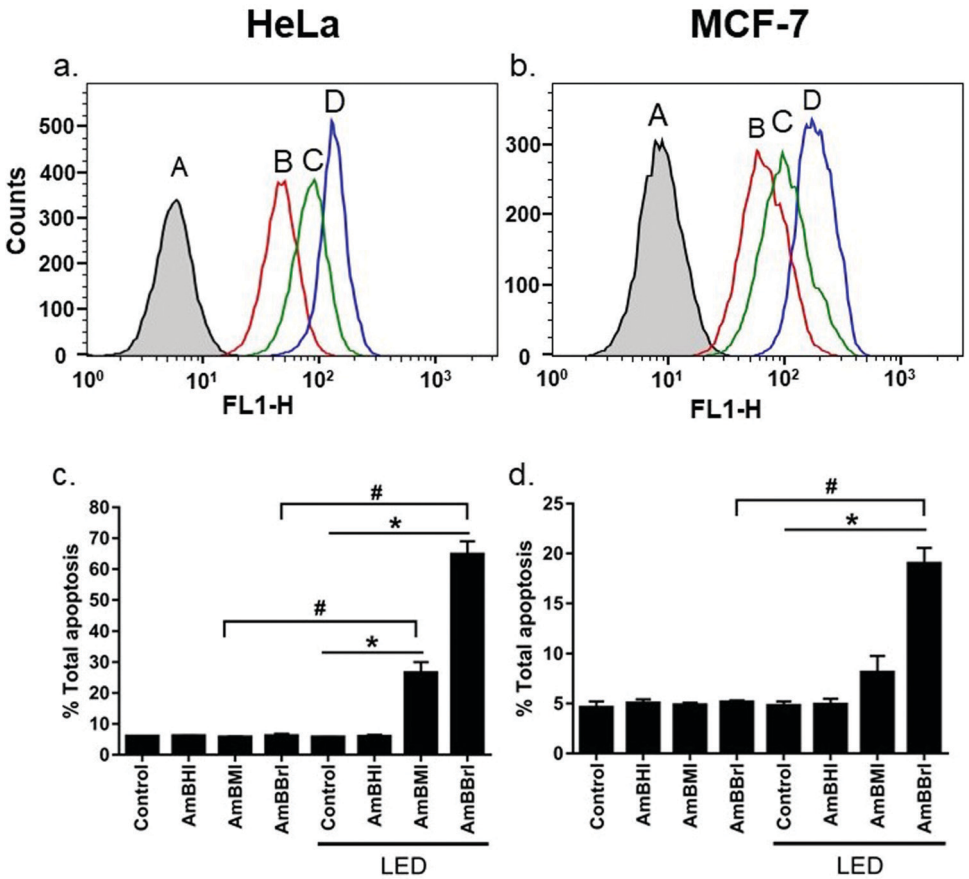

Fig. 6 Plots of cell uptake of AmBXI analyzed by FACS (a and b), where A = control, B = AmBMI, C = AmBBrI, and D = AmBHI. The larger shift in fluorescence intensity indicates higher cellular uptake. Quantification of total apoptotic cell population. Data present mean values and error bars denote standard deviation (n = 3). Statistically significant difference was observed for irradiated dye-treated cells, compared with the irradiated control samples (*, $P < 0.05$) unirradiated dye-treated cells (#), as revealed by one-way ANOVA followed by Bonferroni's multiple comparisons test (c and d).

Table 2 Corrected median fluorescence intensities (MFI) of AmBXI against targeted cancer cell lines

	Control	AmBHI	AmBMI	AmBBrI
HeLa	0.42 ± 0.01	99.73 ± 0.06	90.57 ± 0.06	98.97 ± 0.50
MCF-7	0.40 ± 0.19	99.93 ± 0.06	89.93 ± 0.01	99.13 ± 0.35

light activation of the dyes. The observed cell population was divided into four quadrants where Q1 (PI is positive, Annexin V is negative) means necrotic cells, Q2 (PI is positive, Annexin V is positive) means late apoptotic cells, Q3 (PI is negative, Annexin V is negative) means that cells are healthy and viable, and Q4 (PI is negative, Annexin V is positive) means early apoptotic cells.

Results are shown in Fig. 6c, d and Fig. S4 (ESI†). Under dark conditions, both HeLa and MCF-7 cancer cells treated with AmBXI dyes showed no difference from the control samples, with most of the cells remaining in Q3. However, after photoactivation, AmBMI and AmBBrI induced the cells to undergo apoptosis while AmBHI hardly did, as reflected by the emergence of appreciable cell population in Q2. For HeLa cells, AmBMI showed moderate apoptosis efficacy of 26%, whereas AmBBrI showed the highest efficacy of 65%. Consistent results were found for MCF-7 cells: total apoptosis that AmBMI and AmBBrI caused were 8% and 20%, respectively. Intriguingly, AmBBrI also caused necrosis to MCF-7 cells, as reflected by unusual cell population in Q1. This is probably due to the high concentration of the dye (0.5 μM) and a difference in the response of this cell line.

The results of phototoxicity experiments conducted on AmBXI dyes agree with the results of the $^1O_2$ generation experiments and of the computational studies. The increase in ISC likelihood brought about by the heavy-atom effect of bromine contributed to the phototoxicity of AmBMI and AmBBrI. When BODIPY is used as the platform for PSs, the location of the substituents is known to bear more significance than the number of halogen atoms present in the structure, when it comes to the value of ϕ_Δ.[59] In this case, bromine substitutions at the lateral 2,6-positions rendered the ISC process more likely, thus enhancing the efficiency of the generation of the cytotoxic $^1O_2$. Notably, the introduction of one bromine atom was enough to produce a phototoxic effect. Moreover, as indicated by the results of the cell imaging experiments conducted on

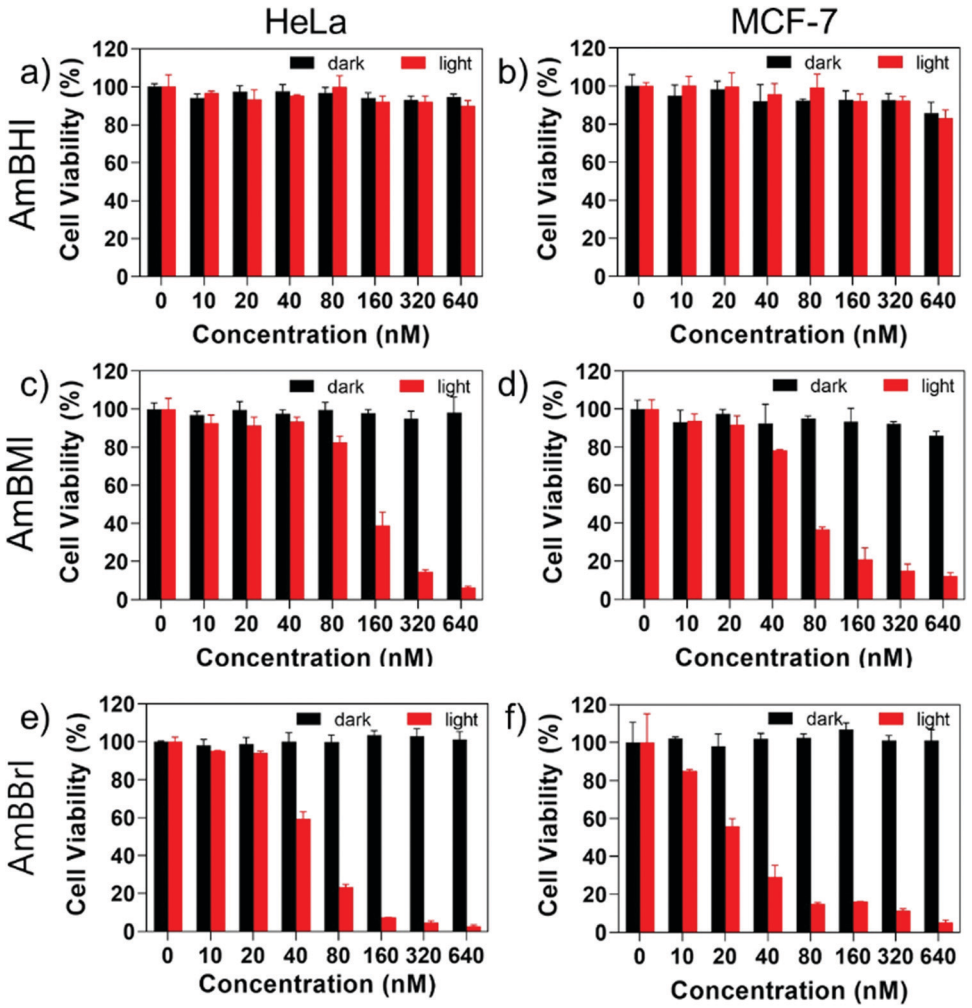

Fig. 7 Results of dose-dependent cell proliferation (MTS) assay conducted on AmBHI, AmBMI and AmBBrI using cervical cancer (HeLa) (a, c and e) and human breast cancer (MCF-7) (b, d and f) cells without and with LED light irradiation at 690 nm for 30 min. Data represent mean values and error bars denote standard deviation (n = 3).

AmBMI and AmBBrI, biological observations may depart from predictions based on theoretical studies due to the influence of the cellular environment.

Conclusion

In developing effective PSs, light penetration depth and target specificity are just as crucial as efficient $^1O_2$ generation. We worked around the shortcomings of BODIPY-based dyes, such as hydrophobicity, absorption in the visible region, and negligible $^1O_2$ generation, to develop the NIR-absorbing and mitochondrion-targeting AmB*X*I PSs. The number of bromine atoms in AmB*X*I dyes can be fine-tuned to achieve a balance between cell imaging and light-controlled cell death. Theoretical studies revealed that the addition of each bromine atom rendered the ISC more likely and increased the ϕ_Δ value. Accordingly, the results of cell viability assays indicate that AmB*X*I dyes exhibited low dark cytotoxicity, while the brominated AmBMI and AmBBrI exhibited phototoxicity, with AmBBrI being characterized by lower IC_{50} values than AmBMI. Surprisingly, AmB*X*I afforded good cell imaging results, despite its low fluorescence quantum yield in aqueous solutions. Interaction between the dye and cellular biomolecules may have increased the structural rigidity of the PS, hampering nonradiative pathways. Finally, the AmB*X*I dyes were observed to accumulate preferentially in the mitochondria of HeLa and MCF-7 cancer cell lines. These results demonstrate the efficacy of using modular structural modifications to access desired photophysical and biological properties of PSs.

Experimental Section

Materials

All reagents were obtained from commercial sources and used without additional purification unless specified. 2,4-Dimethylpyrrole, (4-dimethylamino) benzaldehyde, trifluoroacetic acid and boron trifluoride diethyl etherate ($BF_3{\cdot}Et_2O$) were purchased from Sigma Aldrich (USA). 2,3-Dichloro-5,6-dicyano-1,4-benzoquinone was bought from Alfa Aesar (USA).

N-Bromosuccinimide was obtained from TCI (Japan). Triethylamine (TEA), iodomethane, sodium hydrogen carbonate ($NaHCO_3$), magnesium sulfate ($MgSO_4$) were procured from Daejung Chemical (South Korea). Solvents were of analytical grade and were distilled prior to use. All compounds were characterized by ^{1}H- and ^{13}C-NMR spectroscopy on a Bruker AM 250 spectrometer (USA) and high-resolution electrospray ionization mass spectrometry (HR-ESI-MS) on a SYNAPT G2-Si high-definition mass spectrometer (United Kingdom).

Synthesis

General procedure for the synthesis of 4-dimethylanilino BODIPY 1. BODIPY 1 was prepared following reported literature.[60] 2,4-Dimethylpyrrole (1.5 g, 2.2 eq.) and (4-dimethylamino) benzaldehyde (1.1 g, 1.0 eq.) were dissolved in dry MC at room temperature under argon gas. A catalytic amount of trifluoroacetic acid was added dropwise and the mixture was left stirring overnight. DDQ (1.6 g, 1.0 eq.) was dissolved in dry MC and added dropwise to the mixture at 0 °C and stirred for 2 h. Then, TEA (4.4 g, 6.0 eq.) was added and stirred for 30 min, followed by the dropwise addition of BF_3OEt_2 (6.1 g, 60 eq.) to the reaction. The reaction was stirred for 1.5 h. The reaction was washed with H_2O and MC, dried with magnesium sulfate, filtered, and evaporated to dryness. Purification by column chromatography using hexane/CH_2Cl_2 (1 : 1) resulted to orange crystals. (See Fig. S5, ESI†) (Yield: 243 mg, 9.1%) ^{1}H NMR (300 MHz, $CDCl_3$, 25 °C, TMS): δ = 7.05 (d, 2H, J = 9 Hz; 2Ar-H), 6.76 (d, 2H, J = 9 Hz; 2Ar-H), 5.97 (s, 2H; 2Ar-H), 3.02 (s, 6H; $2CH_3$), 2.55 (s, 6H; $2CH_3$), 1.48 ppm (s, 6H; $2CH_3$).

Mono- and di-bromination of 1. BODIPY 1 was brominated using precise equivalents of *N*-bromosuccinimide: 0.5 eq. for monobromination and 2.5 eq. for dibromination. 1 and *N*-bromosuccinimide were stirred in dry methylene chloride under Argon atmosphere at room temperature until the end of reaction. The solvent was evaporated under reduced pressure followed by purification by column chromatography using hexane/CH_2Cl_2 (2 : 1) elution system.

2. (See Fig. S6, ESI†) 83.0 mg of 1 and 28.0 mg of NBS (Yield: 47.0 mg, 67.2%) ^{1}H NMR (300 MHz, $CDCl_3$, 25 °C, TMS): δ = 7.03 (d, 2H; J = 9 Hz; 2Ar-H), 6.77 (d, 2H; J = 6 Hz; 2Ar-H), 6.02 (s, 1H; Ar-H), 3.03 (s, 6H; $2CH_3$), 2.55 (d, 6H; J = 9 Hz; $2CH_3$), 1.47 ppm (d, 6H; J = 9 Hz; $2CH_3$).

3. (See Fig. S7, ESI†) 43.0 mg of 1 and 61.0 mg of NBS (Yield: 50.0 mg, 61.5%) ^{1}H NMR (300 MHz, $CDCl_3$, 25 °C, TMS): δ = δ = 7.01 (d, 2H; J = 9 Hz; 2Ar-H), 6.77 (d, 2H; J = 9 Hz; 2Ar-H), 3.04 (s, 6H; $2CH_3$), 2.60 (s, 6H; $2CH_3$), 1.49 ppm (s, 6H; $2CH_3$)

Synthesis of triethylene glycol tosylate. Following the reaction procedure from reported literature with slight modifications, triethylene glycol monomethyl ether (5.0 g, 1.0 eq.) was dissolved in 5 mL pyridine.[61] *p*-toluene sulfonyl chloride (6.97 g, 1.2 eq.) was dissolved in anhydrous methylene chloride and added dropwise to the reaction. The reaction was left stirring for 2 days or until reaction completion. The tosylated intermediate compound was obtained after extracting with methylene chloride, washing with 6 M HCl (25 mL) and drying with magnesium sulfate. (See Fig. S8, ESI†) (Yield: 8.6 g, 88.7%) ^{1}H NMR (300 MHz, $CDCl_3$, 25 °C, TMS): δ = 7.78 (d, 2H, J = 9 Hz; 2Ar-H), 7.34 (d, 2H, J = 9 Hz; 2Ar-H), 4.14–4.17 (m, 2H; CH_2), 3.66–3.70 (m, 2H; CH_2), 3.59–3.63 (m, 6H; $3CH_3$), 3.51–3.55 (m, 2H; CH_2), 3.37 (s, 3H; CH_3), 2.45 ppm (s, 3H; Ar-CH_3).

Synthesis of diPEGylated benzaldehyde (4). Triethylene glycol tosylate (8.6 g, 2.5 eq.) was directly used in the next reaction and dissolved in 40 mL DMF. 3,4-Dihydroxybenzaldehyde (1.5, 1.0 eq.) and anhydrous potassium carbonate (6.6, 4.4 eq.) was added, and the reaction was refluxed at 80 °C for 12 h under inert atmosphere. After cooling to room temperature, the reaction was poured into ice cold water and extracted with MC three times, washed with water and brine, and dried with magnesium sulfate. The solvent was evaporated under reduced pressure and the desired compound was isolated after purification using column chromatography with ethyl acetate/MeOH (9 : 1) as elution solvents. (See Fig. S9, ESI†) (Yield: 1.3 g, 28.4%) ^{1}H NMR (300 MHz, $CDCl_3$, 25 °C, TMS): δ = 9.84 (s, 1H; Ar-H), 7.45 (s, 2H; 2Ar-H), 7.04 (s, 1H; Ar-H), 4.24 (m, 4H; $2CH_2$), 3.92 (m, 4H; $2CH_2$), 3.77 (m, 4H; $2CH_2$), 3.37 (s, 6H; $2CH_3$), 3.67 (m, 8H; $4CH_2$), 3.56 ppm (m, 4H; $2CH_2$).

Knoevenagel condensation reaction. The Knoevenagel condensation reaction was carried out based on reported literature with slight modifications.[62] In a round-bottomed flask, the BODIPY dyes (1–3) and the di-PEGylated benzaldehyde derivative 4 (2.5 eq.) were dissolved in 15 mL of DMF, then catalytic amounts of piperidine and acetic acid were added to the reaction under inert conditions. The reaction was refluxed until completion as indicated by the change in color. The solvent was evaporated under reduced pressure. Purification by column chromatography using ethyl acetate/MeOH (9 : 1) and CH_2Cl_2/MeOH (50 : 1) yielded the desired compounds.

5. (See Fig. S10 and S11, ESI†) 53.9 mg of 1 and 189.6 mg of 4 (Yield: 77.0 mg, 44.0%) ^{1}H NMR (300 MHz, $CDCl_3$, 25 °C, TMS): δ = 7.54 (d, 2H; J = 15 Hz; 2Ar-H), 7.24 (s, 1H; Ar-H), 7.19 (s, 1H; Ar-H), 7.12 (m, 3H; 3CH), 7.09 (s, 1H; Ar-H), 6.92 (d, 2H; 2Ar-H), 6.78 (d, 2H; J = 9 Hz; 2Ar-H), 6.61 (s, 2H; 2Ar-H), 4.20–4.27 (m, 8H; $4CH_2$), 3.88–3.92 (m, 8H; $4CH_2$), 3.75–3.80 (m, 8H; $4CH_2$), 3.64–3.71 (m, 16H; $8CH_2$), 3.52–3.58 (m, 8H; $4CH_2$), 3.36–3.39 (d, 12H; J = 9 Hz; $4CH_3$), 3.03 (s, 6H; $2CH_3$), 1.55 ppm (s, 6H; $2CH_3$). ^{13}C NMR (300 MHz, $CDCl_3$, 25 °C, TMS): δ = 151.5, 150.1, 149.1, 143.1, 135.7, 130.7, 129.4, 128.5, 124.0, 123.7, 122.6, 121.5, 114.4, 114.3, 113.9, 113.5, 112.4, 72.0, 71.0, 70.8, 70.7, 70.6, 59.1, 40.4, 15.0 ppm.

6. (See Fig. S12 and S13, ESI†) 38.0 mg of 2 and 89.3 mg of 4 (Yield: 41.0 mg, 37.9%) ^{1}H NMR (300 MHz, $CDCl_3$, 25 °C, TMS): δ = 7.91 (d, 1H; J = 24 Hz; Ar-H), 7.54 (d, 2H; J = 15 Hz; 2Ar-H), 7.29 (m, 1H; Ar-H), 7.25 (m, 1H; CH), 7.20 (d, 1H; J = 3 Hz; CH), 7.12 (d, 2H; J = 9 Hz; 2CH), 7.07 (d, 2H; J = 9 Hz; 2Ar-H), 6.94 (q, 2H; J = 12 Hz; 2Ar-H), 6.91 (d, 1H; J = 9 Hz; Ar-H), 6.78 (d, 2H; J = 9 Hz; 2Ar-H), 6.66 (s, 1H; Ar-H), 4.15–4.27 (m, 8H; $4CH_2$), 3.85–3.91 (m, 8H; $4CH_2$), 3.73–3.78 (m, 8H; $4CH_2$), 3.63–3.70 (m, 16H; $8CH_2$), 3.52–3.58 (m, 8H; $4CH_2$), 3.36–3.39 (m, 12H; $4CH_3$), 3.04 (s, 6H; $2CH_3$), 1.56 (s, 3H; CH_3), 1.52 ppm (s, 3H; CH_3). ^{13}C NMR (300 MHz, $CDCl_3$, 25 °C, TMS): δ = 151.00, 150.0,

149.0, 131.3, 130.2, 129.3, 122.1, 122.0, 121.2, 120.6, 114.5, 112.4, 72.0, 70.9, 70.8, 70.6, 70.0, 69.8, 69.7, 69.2, 69.1, 68.8, 68.7, 59.1, 40.3, 24.6, 15.2, 13.7 ppm.

7. (See Fig. S14 and S15, ESI†) 50.0 mg of 3 and 122.98 mg of 4 (Yield: 59.5 mg, 46.3%) ^{1}H NMR (300 MHz, $CDCl_3$, 25 °C, TMS): δ = 8.02 (d, 2H; J = 18 Hz; 2Ar-H), 7.59 (d, 2H; J = 18 Hz; 2Ar-H), 7.50 (s, 1H; CH), 7.30 (d, 2H; J = 9 Hz; 2CH), 7.15 (s, 2H; 2Ar-H), 7.19 (s, 2H; 2Ar-H), 6.96 (d, 3H; J = 9 Hz; 3Ar-H), 4.23–4.27 (m, 8H; $4CH_2$), 3.89–3.93 (m, 8H; $4CH_2$), 3.75–3.79 (m, 8H; $4CH_2$), 3.64–3.71 (m, 16H; $8CH_2$), 3.53–3.58 (m, 8H; $4CH_2$), 3.35 (d, 12H; J = 9 Hz; $4CH_3$), 2.92 (s, 6H; $2CH_3$), 1.52 ppm (s, 6H; $2CH_3$). ^{13}C NMR (300 MHz, $CDCl_3$, 25 °C, TMS): δ = 153.4, 150.7, 149.1, 139.4, 130.7, 129.7, 121.7, 114.6, 114.4, 72.0, 71.0, 70.8, 70.6, 59.1, 44.2, 29.6, 14.2 ppm.

Quantitative methylation of BODIPY dyes 5–7. Intermediate BODIPY compounds 5 (77.0 mg), 6 (52.0 mg), and 7 (59.5 mg) were dissolved in in 5 mL anhydrous MeCN, respectively. 2.0 mL of iodomethane was added and the mixture was stirred for 2 days at room temperature. The reaction was monitored until completion using TLC.[63] Purification by column chromatography using aluminium oxide with CH_2Cl_2/MeOH (9.5 : 0.5) elution system afforded the final compounds.

AmBHI. (See Fig. S16 and S17, ESI†) (Yield: 76.7 mg, 89.0%) ^{1}H NMR (300 MHz, $CDCl_3$, 25 °C, TMS): δ = 8.00 (d, 2H; J = 9 Hz; 2Ar-H), 7.46–7.52 (m, 4H; 4CH), 7.34 (, 2H; 2Ar-H), 7.16 (s, 4H; 4Ar-H), 6.90 (d, 2H; J = 9 Hz; 2Ar-H), 6.79 (s, 2H; 2Ar-H), 4.86 (s, 9H; $3CH_3$), 4.11–4.12 (m, 8H; $4CH_2$), 3.78–3.81 (m, 8H; $4CH_2$), 3.62–3.68 (m, 8H; $4CH_2$), 3.55–3.62 (m, 16H; $8CH_2$), 3.45–3.51 (m, 8H; $4CH_2$), 3.28–3.31 (d, 12H; J = 9 Hz; $4CH_3$), 1.30 ppm (s, 6H; $2CH_3$). ^{13}C NMR (300 MHz, $CDCl_3$, 25 °C, TMS): δ = 150.5, 149.0, 148.8, 72.0, 70.9, 70.7, 70.6, 69.8, 69.7, 69.2, 68.7, 59.1, 57.7 ppm. HRMS (ESI) m/z calcd for $C_{64}H_{91}BF_2IN_3O_{16}$: 1206.65 [M-I] +; found: 1208.63.

AmBMI. (See Fig. S18 and S19, ESI†) (Yield: 33.1 mg, 72.7%) ^{1}H NMR (300 MHz, $CDCl_3$, 25 °C, TMS): δ = 8.32 (d, 2H; J = 6 Hz; 2Ar-H), 7.95 (d, 1H; J = 18 Hz; Ar-H), 7.61 (d, 2H; J = 9 Hz; 2Ar-H), 7.52 (d, 2H; J = 15 Hz; CH), 7.30 (m, 2H; 2Ar-H), 7.13 (d, 2H; J = 6 Hz; 2Ar-H), 6.94 (m, 2H; 2Ar-H), 6.70 (s, 1H; Ar-H), 4.21–4.27 (m, 8H; $4CH_2$), 4.19 (s, 9H; $3CH_3$), 3.89–3.92 (m, 8H; $4CH_2$), 3.75–3.78 (m, 8H; $4CH_2$), 3.62–3.70 (m, 16H; $8CH_2$), 3.52–3.57 (m, 8H; $4CH_2$), 3.36–3.39 (d, 12H; J = 6 Hz; $4CH_3$), 1.36 ppm (d, 6H; J = 9 Hz; $2CH_3$). ^{13}C NMR (300 MHz, $CDCl_3$, 25 °C, TMS): δ = 151.0, 150.4, 148.9, 148.2, 138.0, 131.4, 130.8, 129.7, 121.4, 71.9, 70.8, 70.7, 70.5, 69.8, 69.7, 69.6, 69.3, 69.2, 68.7, 66.7, 59.0, 57.8, 15.3, 13.8 ppm. HRMS (ESI) m/z calcd for $C_{64}H_{90}BBrF_2IN_3O_{16}$: 1284.56 [M-I] +; found: 1284.56.

AmBBrI. (See Fig. S20 and S21, ESI†) (Yield: 62.0 mg, 94.3%) ^{1}H NMR (300 MHz, $CDCl_3$, 25 °C, TMS): δ = 8.27 (d, 2H; J = 9 Hz; 2Ar-H), 8.04 (d, 2H; J = 18 Hz; 2Ar-H), 7.63 (d, 2H; J = 9 Hz; 2CH), 7.52 (d, 2H; J = 9 Hz; 2CH), 7.30 (d, 2H; J = 9 Hz; 2Ar-H), 7.15 (s, 2H; 2Ar-H), 6.95 (d, 2H; J = 9 Hz; 2Ar-H), 4.21–4.27 (m, 8H; $4CH_2$), 4.18 (s, 9H; $3CH_3$), 3.88–3.96 (m, 8H; $4CH_2$), 3.75–3.78 (m, 8H; $4CH_2$), 3.62–3.70 (m, 16H; $8CH_2$), 3.51–3.57 (m, 8H; $4CH_2$), 3.36–3.39 (d, 12H; $2CH_3$), 1.34 ppm (s, 6H; $2CH_3$). ^{13}C NMR (300 MHz, $CDCl_3$, 25 °C, TMS): δ = 153.4, 150.7, 149.1, 139.4, 130.7, 129.7, 121.7, 114.7, 114.4, 72.0, 71.0, 70.8, 70.7, 70.6, 69.9, 69.8, 69.2, 68.8, 59.1, 44.2, 14.2 ppm. HRMS (ESI) m/z calcd for $C_{64}H_{89}BBr_2F_2IN_3O_{16}$: 1362.47 $[M\text{-}I]^+$; found: 1367.44.

Methods

Steady-state spectroscopic measurements. Steady-state absorption and emission spectra of BODIPY samples dissolved in methanol were measured at room temperature using a LAMBDA 25 spectrophotometer (PerkinElmer) and a LS-55 fluorometer (PerkinElmer), respectively. The relative fluorescence quantum yields (ϕ_F) were determined with Rhodamine 6G (ϕ_F = 0.95 in ethanol) as reference and according to where the superscripts S and R stand for sample and reference, respectively. A, E, and n refer to the absorbance of the solution at the excitation wavelength, the integrated fluorescence intensity, and the refractive index of the solvent used, respectively.

Singlet oxygen quantum yield measurements. The singlet oxygen quantum yields (ϕ_Δ) were determined by a comparative spectrophotometric method using 1,3-diphenylisobenzofuran (DPBF) as $^1O_2$ quencher and methylene blue (MB) as standard (ϕ_Δ = 0.50 in methanol). Air-saturated sample solutions of DPBF ($A_{410nm} \sim 1.0$) containing each of the BODIPY dyes ($A_{660nm} \sim 0.5$) were carefully irradiated by an LED light (λ_{max} = 660 nm) with the illumination intensity of 8 mW cm^{-2}. During the irradiation, the temporal photodegradation of DPBF was monitored by recording the absorption spectra of the solutions every five minutes. Finally, the singlet oxygen quantum yield was calculated by

$$\phi_\Delta^S = \phi_\Delta^R \left(\frac{m_S}{m_R}\right)\left(\frac{F_R}{F_S}\right)$$

where m is the slope of the photodegradation curve and F is the correction factor for the difference in absorbance between sample and reference and is given as $F = 1–10^{-A}$.

To further evaluate $^1O_2$ generation efficiency in aqueous medium, we used water soluble 9,10-anthracenediyl-bis(methylene)dimalonic acid (ABDA) as alternative $^1O_2$ quencher. Water solutions of BODIPY dyes with ABDA were prepared and experiments were conducted following the procedure described above. Higher illumination intensity was employed because, compared to DPBF, ABDA was less sensitive to singlet oxygen.[64]

Quantum chemical calculations. Optimized geometries and electronic states of BODIPY dyes were calculated based on density functional theory (DFT) and time-dependent DFT (TD-DFT), respectively. These calculations were performed under water solvent environment, using the B3LYP functional of the Gaussian 16 program package and the 6-31G(d) basis sets. To evaluate spin–orbit coupling matrix elements, TD-DFT calculations were performed in the ORCA 5.0.1 at the B3LYP/ZORA-def2-TZVP level of theory,[65,66] where ZORA denotes the zero-order relativistic approximation and afforded taking relativistic effects into account. Unless otherwise noted, in all calculations, the peripheral triethylene glycol chains of the BODIPY dyes were replaced by hydrogen atoms to reduce computational costs.

Cells and cell cultures. HeLa (human cervix adenocarcinoma) and MCF-7 (human breast adenocarcinoma) were obtained from the Korean Cell Line Bank. They were maintained in RPMI 1640 medium (Gibco, Carlsbad, CA, USA) supplemented with 10% heat-inactivated fetal bovine serum (FBS) and antibiotics (100 U mL^{-1} penicillin and 100 mg mL^{-1} streptomycin) (Welgene Inc., South Korea) at 37 °C in a humidified 5% CO_2 incubator.

Cell proliferation assay. HeLa and MCF-7 cells (2 × 103 cells per well) were seeded in 96-well plates and incubated at 37 °C in 5% CO_2 for 24 h. Next, the cells were treated with the BODIPY dyes in DMSO at different concentrations for another 24 h. The concentrations employed were 0, 10, 20, 40, 80, 160, 320, and 640 nM. The cell viability was measured following the protocols for CellTiter 96® AQueous One Solution Cell Proliferation Assay (Promega, Madison, WI, USA).[46,47] Then the absorbance was determined at 690 nm using ELISA plate reader (Thermo Fisher Scientific, Inc., Waltham, MA, USA).

Phototoxicity. HeLa and MCF-7 cells (2 × 103 cells per well) were maintained in the same way as described above but with further incubation of 2 h at 37 °C in 5% CO_2 under dark conditions. Then, the media were changed with phenol-red free RPMI 1640 followed by irradiation with red light-emitting diode (LED, 690 nm, 3 mW) for 30 min. The cells were incubated for further 24 h and the cell viability was measured using the same method described above.

Confocal laser scanning microscopy. HeLa cells were treated with the BODIPY dyes (1 μM) for 24 h. Then, they were further incubated with mitochondria-staining MitoTracker Green (Invitrogen) for 45 min. Cells were then fixed with 4% paraformaldehyde for 10 min and permeabilized for 10 min with 0.1% Triton X-100 followed by counterstaining with 4′,6-diamidino-2-phenylindole (DAPI) for 1 h at room temperature. Finally, images of the cells were taken using confocal microscopy (LSM-700, Carl Zeiss, Germany).

Cellular uptake by flow cytometry. HeLa and MCF-7 cells (2 × 105) in 6-well plates were incubated with 0.5 μM of the BODIPY dyes at 37 °C. The cells incubated with DMSO under identical condition were used as control sample. After 2 h of incubation, DMSO or BODIPY dyes-treated cells were collected and analyzed using a FC500 flow cytometer (Beckman Coulter, CA, USA).

Annexin V/PI assay. The Annexin V/PI assay kit (BD Biosciences, San Diego, CA, USA) was used to measure total (early + late) apoptosis according to the manufacturer's instructions. HeLa and MCF-7 cells (2 × 105) were plated in triplicate in 6-well plates and incubated overnight to allow cell attachment. The cells were treated with either DMSO (control) or the BODIPY dyes for 4 h and then irritated with red light-emitting diode (LED, 690 nm, 3 mW) for 30 min. At the end of the treatment, the cells were collected by trypsin treatment, resuspended in Annexin V/PI solution, incubated for 15 min at room temperature with gentle shaking in the dark, and analyzed using a FC500 flow cytometer.

Statistical analysis. All data are expressed as the means ± standard deviations and were compared by one-way analysis of variance and Tukey's test, using Prism GraphPad 6 software (San Diego, CA, USA). Group means were considered as significantly different at $p < 0.05$.

Author information

Jaesung Yang – Department of Chemistry, Yonsei University, 1 Yonseidae-Gil, Wonju, Gangwon 26493, Korea; E-mail: jaesung.yang@yonsei.ac.kr; Ho-Joong Kim – Department of Chemistry, Chosun University, 309 Pilmun-daero, Dong-gu, Gwangju 61452, Korea; e-mail: hjkim@chosun.ac.kr; Joomin Lee – Department of Food and Nutrition, Chosun University, 309 Pilmun-daero, Dong-gu, Gwangju 61452, Korea; e-mail: joominlee@chosun.ac.kr; Isabel Wen Badon – Department of Chemistry, Chosun University, 309 Pilmun-daero, Dong-gu, Gwangju 61452, Korea; Chanwoo Kim – Department of Chemistry, Yonsei University, 1 Yonseidae-Gil, Wonju, Gangwon 26493, Korea; Jong Min Lim – Center for Molecular Spectroscopy and Dynamics, Institute for Basic Science (IBS), 145 Anam-ro, Seongbuk-gu, Seoul 02841, Korea; Duy Khuong Mai – Department of Chemistry, Chosun University, 309 Pilmun-daero, Dong-gu, Gwangju 61452, Korea; Temmy Pegarro Vales – Department of Natural Sciences, Caraga State University, KM7 NH1, Butuan City 8600, Philippines; Dongho Kang – Department of Chemistry, Yonsei University, 1 Yonseidae-Gil, Wonju, Gangwon 26493, Korea; Sung Cho – Department of Chemistry, Chonnam National University, 99 Daehak-ro, Yuseong-gu, Gwangju 61186, Korea;

Conflicts of interest

The authors declare no competing financial interests.

Acknowledgements

The work at Chosun University was supported by Basic Science Research Program through the National Research Foundation of Korea (NRF) (2020R1F1A1071784). The work at Yonsei University was supported by the NRF grant funded by the Korea government (MSIT) (No. 2019R1G1A109926913).

References

1 P. Agostinis, K. Berg, K. A. Cengel, T. H. Foster, A. W. Girotti, S. O. Gollnick, S. M. Hahn, M. R. Hamblin, A. Juzeniene, D. Kessel, M. Korbelik, J. Moan, P. Mroz, D. Nowis, J. Piette, B. C. Wilson and J. Golab, *Ca-Cancer J. Clin.*, 2011, **61**, 250–281.
2 X. Zhao, J. Liu, J. Fan, H. Chao and X. Peng, *Chem. Soc. Rev.*, 2021, **50**, 4185–4219.
3 M. Tarstedt, M. Gillstedt, A. M. Wennberg Larkö and J. Paoli, *J. Eur. Acad. Dermatol. Venereol.*, 2016, **30**, 420–423.
4 A. K. D'Cruz, M. H. Robinson and M. A. Biel, *Head Neck*, 2004, **26**, 232–240.

5 J. Usuda, S. Ichinose, T. Ishizumi, H. Hayashi, K. Ohtani, S. Maehara, S. Ono, H. Honda, N. Kajiwara, O. Uchida, H. Tsutsui, T. Ohira, H. Kato and N. Ikeda, *Clin. Cancer Res.*, 2010, **16**, 2198–2204.
6 J. P. Celli, B. Q. Spring, I. Rizvi, C. L. Evans, K. S. Samkoe, S. Verma, B. W. Pogue and T. Hasan, *Chem. Rev.*, 2010, **110**, 2795–2838.
7 B. W. Henderson and T. J. Dougherty, *Photochem. Photobiol.*, 1992, **55**, 145–157.
8 N. E. Aksakal, E. Tanrıverdi Eçik, H. H. Kazan, G. Yenilmez Çiftçi and F. Yuksel, *Photochem. Photobiol. Sci.*, 2019, **18**, 2012–2022.
9 E. Ruggiero, S. Alonso-deCastro, A. Habtemariam and L. Salassa, *Dalton Trans.*, 2016, **45**, 13012–13020.
10 G. Ulrich, R. Ziessel and A. Harriman, *Angew. Chem., Int. Ed.*, 2008, **47**, 1184–1201.
11 T. Kowada, H. Maeda and K. Kikuchi, *Chem. Soc. Rev.*, 2015, **44**, 4953–4972.
12 S. P. Singh and T. Gayathri, *Eur. J. Org. Chem.*, 2014, 4689–4707.
13 J. Bañuelos, *Chem. Rec.*, 2016, **16**, 335–348.
14 Y. H. Jung, D. Karthik, H. Lee, J. H. Maeng, K. J. Yang, S. Hwang and J. H. Kwon, *ACS Appl. Mater. Interfaces*, 2021, **13**, 17882–17891.
15 Z. Ruan, Y. Zhao, P. Yuan, L. Liu, Y. Wang and L. Yan, *J. Mater. Chem. B*, 2018, **6**, 753–762.
16 Q. Wang, D. K. P. Ng and P.-C. Lo, *J. Mater. Chem. B*, 2018, **6**, 3285–3296.
17 H. Chen, Q. Bi, Y. Yao and N. Tan, *J. Mater. Chem. B*, 2018, **6**, 4351–4359.
18 P. Majumdar, X. Yuan, S. Li, B. Le Guennic, J. Ma, C. Zhang, D. Jacquemin and J. Zhao, *J. Mater. Chem. B*, 2014, **2**, 2838–2854.
19 D. Khuong Mai, B. Kang, T. Pegarro Vales, I. W. Badon, S. Cho, J. Lee, E. Kim and H.-J. Kim, *Molecules*, 2020, **25**, 3340.
20 V.-N. Nguyen, Y. Yim, S. Kim, B. Ryu, K. M. K. Swamy, G. Kim, N. Kwon, C.-Y. Kim, S. Park and J. Yoon, *Angew. Chem., Int. Ed.*, 2020, **59**, 8957–8962.
21 A. J. Sánchez-Arroyo, E. Palao, A. R. Agarrabeitia, M. J. Ortiz and D. García-Fresnadillo, *Phys. Chem. Chem. Phys.*, 2017, **19**, 69–72.
22 M. Bröring, R. Krüger, S. Link, C. Kleeberg, S. Köhler, X. Xie, B. Ventura and L. Flamigni, *Chemistry*, 2008, **14**, 2976–2983.
23 Y. Ni and J. Wu, *Org. Biomol. Chem.*, 2014, **12**, 3774–3791.
24 T. Uppal, X. Hu, F. R. Fronczek, S. Maschek, P. Bobadova-Parvanova and M. G. H. Vicente, *Chem. – Eur. J.*, 2012, **18**, 3893–3905.
25 X.-D. Jiang, R. Gao, Y. Yue, G.-T. Sun and W. Zhao, *Org. Biomol. Chem.*, 2012, **10**, 6861–6865.
26 T. Bura and R. Ziessel, *Org. Lett.*, 2011, **13**, 3072–3075.
27 S. Zhu, J. Zhang, G. Vegesna, F.-T. Luo, S. A. Green and H. Liu, *Org. Lett.*, 2011, **13**, 438–441.
28 D. G. Rudmann, *Toxicol. Pathol.*, 2013, **41**, 310–314.
29 C. H. Wong, K. W. Siah and A. W. Lo, *Biostatistics*, 2018, **20**, 273–286.
30 A. Lin, C. J. Giuliano, A. Palladino, K. M. John, C. Abramowicz, M. L. Yuan, E. L. Sausville, D. A. Lukow, L. Liu, A. R. Chait, Z. C. Galluzzo, C. Tucker and J. M. Sheltzer, *Sci. Transl. Med.*, 2019, **11**, eaaw8412.
31 J. Neuzil, L. F. Dong, J. Rohlena, J. Truksa and S. J. Ralph, *Mitochondrion*, 2013, **13**, 199–208.
32 T. A. Tabish and M. R. Hamblin, *Biomater. Biosyst.*, 2021, **3**, 100023.
33 H. M. McBride, M. Neuspiel and S. Wasiak, *Curr. Biol.*, 2006, **16**, R551–560.
34 S. E. Weinberg and N. S. Chandel, *Nat. Chem. Biol.*, 2015, **11**, 9–15.
35 F. Sivandzade, A. Bhalerao and L. Cucullo, *Bio-Protoc.*, 2019, **9**, e3128.
36 B. Sui, S. Tang, A. W. Woodward, B. Kim and K. D. Belfield, *Eur. J. Org. Chem.*, 2016, 2851–2857.
37 T. Gao, H. He, R. Huang, M. Zheng, F.-F. Wang, Y.-J. Hu, F.-L. Jiang and Y. Liu, *Dyes Pigm.*, 2017, **141**, 530–535.
38 K. Kirakci, J. Zelenka, M. Rumlová, J. Cvačka, T. Ruml and K. Lang, *Biomater. Sci.*, 2019, **7**, 1386–1392.
39 D. Chen, J. Zhang, Y. Tang, X. Huang, J. Shao, W. Si, J. Ji, Q. Zhang, W. Huang and X. Dong, *J. Mater. Chem. B*, 2018, **6**, 4522–4530.
40 Q. Hu, M. Gao, G. Feng and B. Liu, *Angew. Chem., Int. Ed.*, 2014, **53**, 14225–14229.
41 J. Sun, X. Li, K. Du and F. Feng, *Chem. Commun.*, 2018, **54**, 9194–9197.
42 Y. Zhang, L. Wang, Q. Rao, Y. Bu, T. Xu, X. Zhu, J. Zhang, Y. Tian and H. Zhou, *Sens. Actuators, B*, 2020, **321**, 128460.
43 D. P. Murale, M. M. Haque, S. C. Hong, S.-Y. Jang, J. H. Lee, S. J. An and J.-S. Lee, *Dyes Pigm.*, 2021, **196**, 109830.
44 O. Karaman, T. Almammadov, M. Emre Gedik, G. Gunaydin, S. Kolemen and G. Gunbas, *ChemMedChem*, 2019, **14**, 1879–1886.
45 H. Kang, Y. Si, Y. Liu, X. Zhang, W. Zhang, Y. Zhao, B. Yang, Y. Liu and Z. Liu, *J. Phys. Chem. A*, 2018, **122**, 5574–5579.
46 A. Loudet and K. Burgess, *Chem. Rev.*, 2007, **107**, 4891–4932.
47 Z. Lou, Y. Hou, K. Chen, J. Zhao, S. Ji, F. Zhong, Y. Dede and B. Dick, *J. Phys. Chem. C*, 2018, **122**, 185–193.
48 Y. Cakmak, S. Kolemen, S. Duman, Y. Dede, Y. Dolen, B. Kilic, Z. Kostereli, L. T. Yildirim, A. L. Dogan, D. Guc and E. U. Akkaya, *Angew. Chem., Int. Ed.*, 2011, **50**, 11937–11941.
49 H. Chong, E. Fron, Z. Liu, S. Boodts, J. Thomas, J. N. Harvey, J. Hofkens, W. Dehaen, M. Van der Auweraer and M. Smet, *Chem. – Eur. J.*, 2017, **23**, 4687–4699.
50 C. Dolan, A. Byrne, C. Long, K. Czamara, A. Kaczor, M. Baranska and T. E. Keyes, *RSC Adv.*, 2017, **7**, 43743–43754.
51 Y.-L. Chen, S.-W. Li, Y. Chi, Y.-M. Cheng, S.-C. Pu, Y.-S. Yeh and P.-T. Chou, *ChemPhysChem*, 2005, **6**, 2012–2017.
52 M. Kasha, *Discuss. Faraday Soc.*, 1950, **9**, 14–19.
53 Y. Dong, P. Kumar, P. Maity, I. Kurganskii, S. Li, A. Elmali, J. Zhao, D. Escudero, H. Wu, A. Karatay, O. F. Mohammed and M. Fedin, *Phys. Chem. Chem. Phys.*, 2021, **23**, 8641–8652.
54 Q. Lin and D. Buccella, *J. Mater. Chem. B*, 2018, **6**, 7247–7256.

55 N. Dorh, S. Zhu, K. B. Dhungana, R. Pati, F.-T. Luo, H. Liu and A. Tiwari, *Sci. Rep.*, 2015, **5**, 18337.
56 L. Biasutto, L. F. Dong, M. Zoratti and J. Neuzil, *Mitochondrion*, 2010, **10**, 670–681.
57 G. Bagkos, K. Koufopoulos and C. Piperi, *Med. Hypotheses*, 2014, **83**, 175–181.
58 H. He, D. W. Li, L. Y. Yang, L. Fu, X. J. Zhu, W. K. Wong, F. L. Jiang and Y. Liu, *Sci. Rep.*, 2015, **5**, 13543.
59 R. Prieto-Montero, A. Prieto-Castañeda, R. Sola-Llano, A. R. Agarrabeitia, D. García-Fresnadillo, I. López-Arbeloa, A. Villanueva, M. J. Ortiz, S. de la Moya and V. Martínez-Martínez, *Photochem. Photobiol.*, 2020, **96**, 458–477.
60 M. L. Agazzi, M. B. Ballatore, E. Reynoso, E. D. Quiroga and E. N. Durantini, *Eur. J. Med. Chem.*, 2017, **126**, 110–121.
61 X. Shi, L. Tan, J. Xing, F. Cao, L. Chen, Z. Luo and Y. Wang, *J. Appl. Polym. Sci.*, 2013, **128**, 1995–2002.
62 J. Zhang, M. Yang, C. Li, N. Dorh, F. Xie, F.-T. Luo, A. Tiwari and H. Liu, *J. Mater. Chem. B*, 2015, **3**, 2173–2184.
63 T. Papalia, G. Siracusano, I. Colao, A. Barattucci, M. C. Aversa, S. Serroni, G. Zappalà, S. Campagna, M. T. Sciortino, F. Puntoriero and P. Bonaccorsi, *Dyes Pigm.*, 2014, **110**, 67–71.
64 T. Entradas, S. Waldron and M. Volk, *J. Photochem. Photobiol., B*, 2020, **204**, 111787.
65 F. Neese, *Wiley Interdiscip. Rev.: Comput. Mol. Sci.*, 2012, **2**, 73–78.
66 F. Neese, *Wiley Interdiscip. Rev.: Comput. Mol. Sci.*, 2018, **8**, e1327.